GSA Data Repository 2018022

Mondy, et al., 2018, The role of asthenospheric flow during rift propagation and breakup: Geology, https://doi.org/10.1130/G39674.1.

Contents

SUPPLEMENTAL METHODS

We solve the problem of conservation of mass, momentum and energy for incompressible mantle flow and lithosphere deformation, using Underworld - an open source particle-in-cell finite-element code (freely available at underworldcode.org), in conjunction with the *Lithospheric Modelling Recipe* (https://github.com/OlympusMonds/lithospheric_modelling_recipe), an open-source python wrapper developed within the EarthByte group to quickly and easily setup and run *Underworld* models in both 2D and 3D.

We assume a visco-plastic rheology depending on temperature, stress, strain, strain rate, and in some experiments melt fraction (see Table DR1). The densities of all rocks depend on temperature (see Table DR1).

Experimental setup

The experiments are run within a Cartesian box of 500 km (x-axis) by 1000 km (y-axis) and 180 km vertically (z-axis). The computational grid dimensions for solving the visco-plastic Stokes problem is 254×512×96 (~2 km cells). A 20 km wide and 8 km deep wedge of lower crust runs along the entire length of the experiment, to preferentially localise deformation in the centre of the domain (Van Wijk and Blackman, 2005). A free-slip boundary condition is imposed to the front and back walls, while a constant pressure is maintained at the bottom of the experiment to simulate the conditions of isostatic equilibrium. The topographic surface, which stands at sea level before rifting, evolves freely beneath a 20 km thick "sticky-air" layer (Crameri et. al., 2012). An initial random plastic strain (up to 5%) is imposed the upper crust to promote strain localisation near the surface.

Fundamental equations

Underworld solves the incompressible equations of continuity for momentum, energy, and mass as below:

$$\frac{\partial \tau_{ij}}{\partial x_j} - \frac{\partial \rho}{\partial x_i} = -\rho g \lambda_i$$

$$\frac{\partial T}{\partial t} + u_i \frac{\partial T}{\partial x_i} = \frac{\partial}{\partial x_i}\left(\kappa \frac{\partial T}{\partial x_i}\right) + Q$$

$$\frac{\partial u_i}{\partial x_i} = 0$$

Where x_i are the spatial coordinates, u_i is the velocity, T is temperature, ρ is density, g is gravity, λ_i is the unit vector in the direction of gravity, t is time, κ is thermal diffusivity, and Q is a source term for the energy equation. Summation on repeated indices is assumed.

Additional terms can be incorporated into the above equations. In the experiments presented, only radiogenic heating is added, unless explicitly mentioned otherwise - however, an additional experiment was run with partial melting, and so the associated terms and values are described below.

Both radiogenic heating and the thermal aspects of partial melting are incorporated into the energy equations as:

$$Q_{\text{radiogenic}} = \frac{A}{\rho C_p}$$

$$Q_{\text{partial melt}} = -1 \times \frac{L_f}{C_p} \frac{\delta M_f}{\delta t}$$

Where A is the rate of radiogenic heat production, C_p is heat capacity, L_f is latent heat of fusion, and M_f is the melt fraction.

The density of a material is defined via a function that depends on temperature and the melt fraction:

$$\rho = \rho_r \times (1 - \alpha(T - T_r) - (M_f \times M_{\Delta\rho_r}))$$

Where ρ_r is reference density, α is thermal expansivity, T_r is reference temperature, and $M_{\Delta\rho_r}$ is the fraction of density change when melted.

The melt fraction is calculated dynamically as part of the experiment, by using the super-solidus formula given by McKenzie and Bickle (1988):

$$SS = \frac{(T - T_s)}{(T_l - T_s)} - 0.5$$

$$M_f = 0.5 + SS + (SS^2 - 0.25) \times (0.4256 + 2.988 \times SS)$$

Where SS is the normalised super-solidus temperature, T_s is the solidus, and T_l is the liquidus.

The solidus and liquidus are defined as:

$$T_s = t_1 + t_2 P + t_3 P^2$$

Where P is pressure, t_1, t_2, and t_3 are defined Table DR1.

The constitutive behaviour is assumed to be visco-plastic rheologies. For the viscous component, flow is computed using dislocation creep (Hirth and Kohlstedt, 2003):

$$\dot{\varepsilon}_{\text{disc}} = A\sigma^n d^{-p} f_{H_2O}^r \exp\left(-\frac{E + PV}{nRT}\right)$$

Where $\dot{\varepsilon}$ is the effective strain-rate, A is the pre-exponential factor, n is the stress exponent, d is the grain-size, p is the grain-size exponent, f_{H2O} is the water fugacity, r is the water fugacity exponent, E is the activation energy, P is the pressure, V is the activation volume, R is the gas constant, and T is the temperature.

For the plastic component, failure is determined using the Drucker-Prager model:

$$\sqrt{J_2} = Ap + B$$

Where $\sqrt{J_2}$ is the second invariant of the deviatoric stress tensor, p is the pressure, and A and B are defined as:

$$A = \frac{2sin\phi}{\sqrt{3}(3 - sin\phi)}$$

$$B = \frac{6Ccos\phi}{\sqrt{3}(3 - sin\phi)}$$

Where C is the cohesion, and ϕ is the friction coefficient.

A linear strain-softening function is applied to the plastic component. As strain is accumulated from 0 to 20%, the material linearly weakens from its original cohesion and friction coefficient to their softened equivalents (defined in see Table DR1). Once fully weakened, the cohesion and friction coefficient remain constant at the softened values.

A stress limiter is applied to all rheologies, to limit the total strength of the lithosphere. The stress limiter is based on the work flow from Watremez et al. (2013), where a Von Mises criterion is applied, where:

$$\sqrt{J_2} = C$$

All materials are limited to 300 MPa in strength via this method, to account from pseudo-plastic processes, such as Peierls creep, and to ensure the lithosphere does not become artificially strong (Demouchy et. al., 2013; Zhong and Watts, 2013). To ensure numerical stability, all rock materials also have a minimum and maximum viscosity range of 1e19 Pa.s to 5e23 Pa.s.

Partial melting has a mechanical effect, whereby material undergoing melt will reduce in viscosity, within a given melt fraction range (defined in Table DR1), based on the following model:

$$\eta_{melted} = \eta \times (1 \times M_{f\%} + \eta_{factor} \times (1 - M_{f\%})$$

Where η_{melted} is the viscosity after melting, η is the viscosity calculated from the flow law, $M_{f\%}$ is a normalised linear interpolation of the melt fraction between the lower and upper limits of the melt fraction range, and η_{factor} is the melt viscous softening factor the material undergoes once fully melted.

Time stepping

Time stepping in *Underworld* uses the Courant-Friedrichs-Lewy (CFL) condition to ensure stable convergence. The CFL is a function of grid size, absolute maximum velocity, and maximum diffusivity. On top of this, to ensure a numerically efficient and temporally stable model run, the computed CFL timestep is multiplied by a factor of 0.33.

Rheologies

The rheologies used are based on published work: the upper crust flow law is a wet quartzite from Paterson and Luan (1990); the lower crust flow law is a mafic granulite from Wang et. al (2012); and the lithospheric mantle flow law is a wet olivine from Hirth and Kohlstedt (2003). Viscous flow laws that use 0 for the water fugacity exponent typically have this effect incorporated into the pre-exponential factor. Radiogenic heat production values are from Hasterok and Chapman (2011). Melt and other parameters derived from Rey and Müller, 2010. The air material uses an isoviscous 1e18 Pa.s flow law, with a density of 1 kg m^{-3}, thermal expansivity of 0 K^{-1}m, and a heat capacity of 1000 J K^{-1}. See Table DR1 for detailed parameters values.

Boundary conditions

Kinematic boundary conditions

At the time of writing, *Underworld1* is only capable of modelling Cartesian domains, which therefore imposes that it cannot natively model the natural system of rifting near a pole of rotation on a sphere. To apply a velocity boundary condition only to the walls of the domain, and allow the internal geodynamics to react freely, the mesh must be projected from spherical to Cartesian as shown in Figure DR5. The stereographic projection of the mesh shows that divergent velocity increases as a linear function of distance from the Euler pole, and small

circles have constant divergent velocity along their length. Imposed velocities applied at the boundary of the model are parallel to the small circles. When the mesh is projected into the Cartesian coordinates in *Underworld*, these properties are preserved - divergent velocities increase as a function of distance from the pole, and are parallel to small circles. Note that the approximation of a linear increase of velocity from the pole is valid when close to the Euler pole - over the model domain, the linear gradient deviates from the Euler pole derived velocity by less than 2%.

Other Cartesian numerical experiments featuring nearby Euler poles of rotation, e.g., Ellis et. al., 2011, differ from our method by instead applying boundary conditions with a velocity component along the *y* axis (that is, the imposed velocities have an *x* and *y* component), consistent with flattening the small circle onto a 2D plane. We did not take this approach, since it both enforces a flow towards the Euler pole of rotation to maintain the same amount of volume in the model domain, and does not necessarily impose velocities parallel to the small circles. Our approach avoids these issues, but instead suffers from implicit mesh distortion nearer to the Euler pole (as shown in the Figure DR5B stereographic projection). Therefore, we ignore the results shown overly distorted cells, shown in faded blue.

Another issue caused by this approximation is an induced shear velocity component that comes from the stretching of the boundary over time (Figure DR5A). This stretching is minimal, accounting for less than 1% of stretching during the experiment runtime. Additional experiments run further away from the Euler pole (see section "Experiment Sensitivity and Robustness", experiment AE5) suffer even less from this distortion and observer the same behaviours, and so the effect is ignored.

Top-surface boundary condition

To emulate a free surface, the models all use an air layer. The air material cannot be modelled at natural values of viscosity or thermal expansivity, since it would be numerically very expensive and unstable. A common substitute is to use a "sticky-air" layer, which has unrealistically high viscosity, but is low enough to not interfere with underlying geodynamics. The isostatic criterion formula from Crameri et. al, 2012 (eq 12) gives a criterion for determining the thickness and viscosity of a good sticky-air layer. Based on this, our experiments use an air-layer with a viscosity of 1e18 Pa.s, and a thickness of 20 km.

Thermal model setup

The top wall of the model domain is held constant at 293.15 K (20°C), and the bottom wall is held at 1623.15 K (1350°C). The model is then thermally equilibrated for ~1 billion years to achieve a steady state geotherm. The experiments use a sticky-air layer to allow the topographic surface to evolve freely. The thermal diffusivity of the air is 2.2e-5 $m^2 s^{-1}$, versus 1e-6 $m^2 s^{-1}$ for rock materials. The high thermal diffusivity of air limits the energy solver time stepping as follows:

$$\Delta t < C \frac{(\Delta x)^2}{K},$$

where Δt is the timestep in seconds, C is the courant factor, Δx is the minimum width of an element, and K is the maximum value of the thermal diffusivity. This implies that using a thermal diffusivity of 2.2e-5 $m^2 s^{-1}$ for the air would impose a Δt of 4.5% the potential maximum if the air material was not present. Since this approach imposes a large computational cost, we instead allow the air material to have a thermal diffusivity of 1e-6 $m^2 s^{-1}$, and then impose an internal thermal boundary condition of 293.15 K in the initial shape of the air material. This approach has been validated with 2D experiments of rifting under

similar conditions and has a negligible effect on model results.

Experiment Sensitivity and Robustness

To ensure the results presented are robust, a number of additional experiments were run. The experiments presented in the main body are very computationally demanding, with each experiment taking ~50,000 CPU hours. Therefore, to enable more rapid exploration of the parameter space, most of the additional experiments were run at 4 km grid cell resolution (half that of the original experiment). To be able to compare the lower resolution experiments to those in the main body (shown on Figure DR4 as **O1**), a 4 km grid cell version of the experiment (**AE1**) was run to confirm that the processes presented are not a function of numerical resolution. All experiments are shown in Figure DR4.

AE2 - Testing the basal boundary condition (4 km resolution): Underworld models isostasy via a function that calculates the local Pratt isostasy at each grid node along the bottom boundary, and applies the appropriate velocity to maintain a constant pressure. To ensure that the boundary condition is not overwhelming the internal geodynamics, an experiment with a 60 km deeper domain (originally 160 km extended to 220 km) was run, with the assumption that the hot, weak asthenosphere will act as a buffer to the basal boundary condition. The thermal initial condition is modified so that additional asthenosphere included in the domain is set to 1623.15°K.

AE3 - With partial melting (4 km resolution): To ensure the thermo-mechanical effects of partial melt (density change, viscosity change, and latent heat of fusion) were not a critical controlling factor, the partial melt functions were enabled in this experiment.

AE4 - No-slip velocity on kinematic walls (4 km resolution): To identify the significance of the velocity boundary conditions on the kinematically driven walls, an experiment where no shear motion along the kinematically driven boundaries was allowed was run.

AE5/AE6 - Halving/Doubling the angular velocity of the Euler pole (2 km resolution): To test if this effect is robust between different velocities, the O1 experiment was modified by halving and doubling the angular rate of extension – functionally increasing or decreasing the distance to the Euler pole. The linear velocities are 0.25 to 2.5 cm/yr for AE5, and 1.0 to 10.0 cm/yr for AE6. The results presented on Figure DR4 are scaled in time so that each timestep displays the same amount of kinematic extension, so they are comparable to other experiments.

To verify the basal boundary condition was behaving appropriately, two post-processing tests were done. The first test was to ensure the pressure across the bottom surface of the domain remained constant, given the Pratt isostasy condition. To check this, the variation of pressure of the bottom surface of the model domain was computed through time. The result was a maximum variation of total lithostatic pressure of 0.4% through the model evolution, which we deemed acceptable. The second test was to ensure that the same amount of material entering the model domain from the basal isostasy condition was equivalent to the amount of material leaving the domain from the kinematic boundary conditions. If any deviation exists, it may imply that the basal boundary condition is forcing some aspect of the geodynamics, rather than reacting to them. The result was a deviation less than 0.063% over the experiment lifetime, once the topographic evolution was taken into account, which we deemed acceptable.

Earthquake Focal mechanisms

Earthquake focal mechanisms displayed on Figure 4 were extracted from the Global CMT Catalogue (http://www.globalcmt.org/CMTsearch.html) (Dziewonski et. al., 1981; Ekström et. al., 2012). We selected events with a magnitude larger than 5.0 between 1976 and 2017. We did subset the catalog records using the tension and null axis plunge search fields. Thrust faults (in red) have large plunge (> 45) of tension axis, strike-slip faults (green) have large plunge of null axis, and normal faults (blue) have small plunge (< 45) for both tension and null axes.

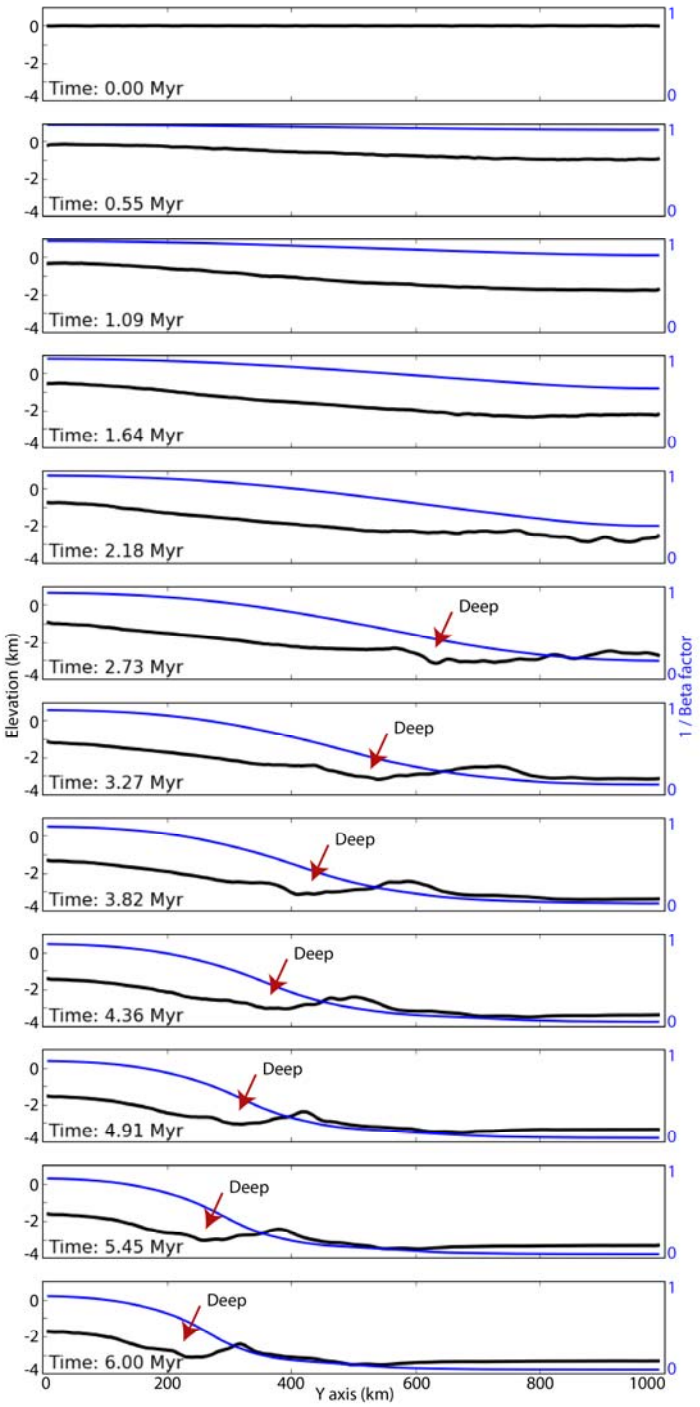

Figure DR1. Temporal evolution of topography and crustal thinning along the rift of the rotational experiment. The elevation along the rift axis shows the formation and migration of a "Deep", a localized topographic dip ahead of the rift tip. The formation of the deep begins when the lithospheric thickness is reduced by half, and tends to follow this point up the margin (towards y = 0 km). Once break-up has occurred (where 1/Beta is ~0), the elevation stabilises around 3.6 km depth. The deep ahead of the rift tip is similar to the Hess Deep described by Floyd et al., 2002 in the Galapagos Rise.

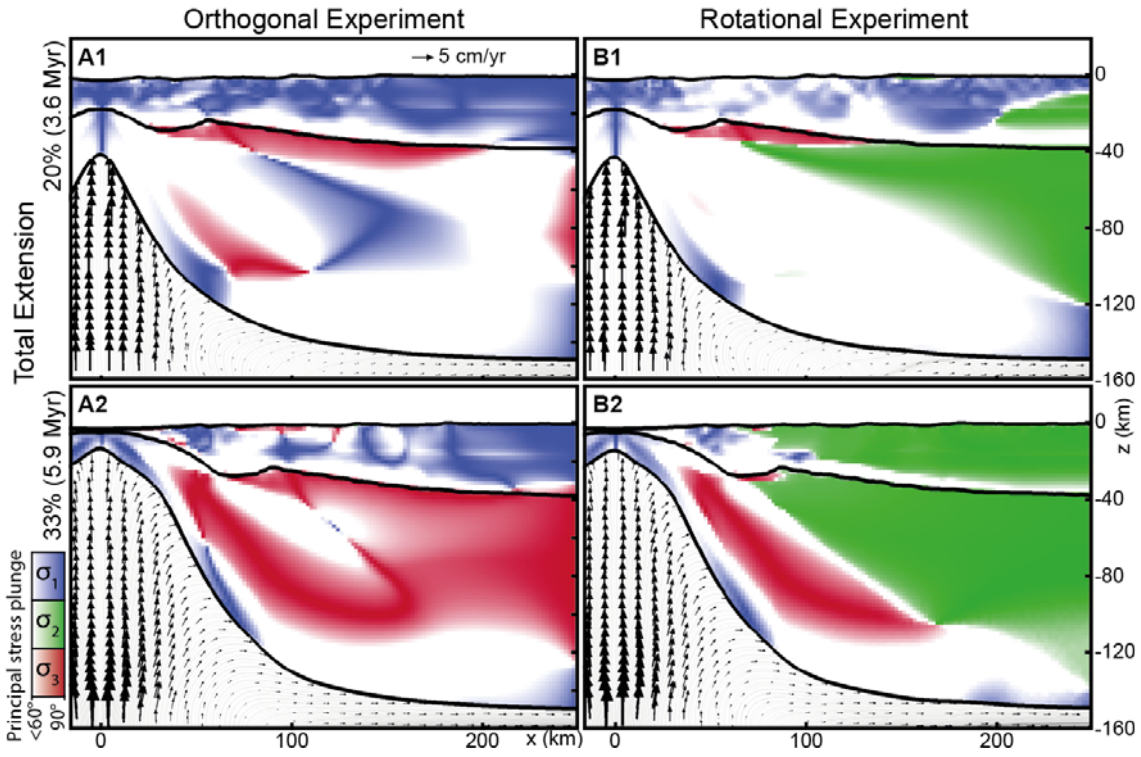

Figure DR2. Stress regime changes throughout the lithosphere. Mapping of Andersonian-like stress regimes (i.e. the plunge of one of the principal stress axes is > 60º) on cross-sections perpendicular to rift axis at y = 500 km. The **orthogonal** experiment shows that extensional stress regime (in blue) largely dominates the lithosphere in the early stages of the experiment **(A1**), with only the surficial part of the axial rift graben and the very base of the lithosphere, directly above the upwelling asthenospheric dome, under compression. As the lithosphere continues to thin and reaches breakup (**A2**) the stress regime becomes strongly partitioned. Compression (in red) dominates in the lithospheric mantle, whereas extension dominates in the crust, though some compression persists along the continental margins. The **rotational** experiment (**B1** and **B2**) shows similar lithospheric structure, but instead with large areas dominated by strike-slip stress regime.

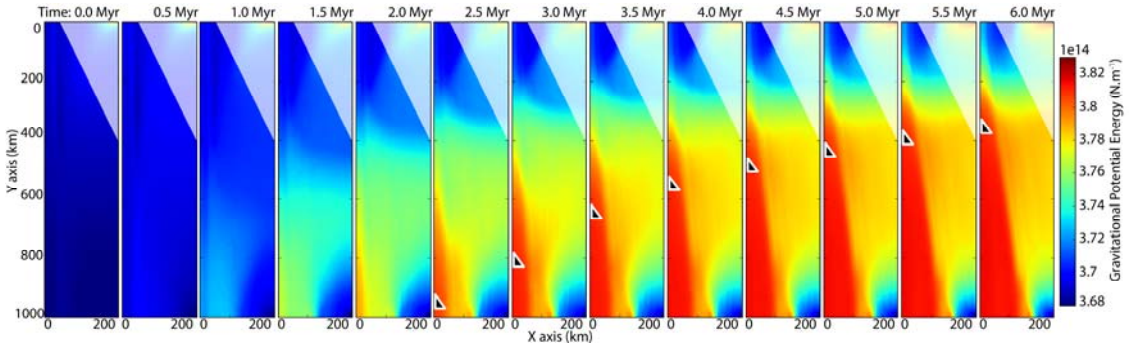

Figure DR3. Mapping the evolution of gravitational potential energy (GPE) during rotational rifting. As lithospheric thinning occurs, an excess of GPE within the rift centre builds as heavier mantle material displaces the lighter crust. Since the rifting occurs much faster further from the Euler pole, it produces a gradient of GPE along the x and y axes away from the forming asthenospheric dome. Only half the domain is shown (X = 0 to X = 250 km), since it is symmetrical. GPE was calculated by vertical integration of the lithostatic pressure. Black triangles represent the rift tip, where $1/\beta < 0.2$ (see Fig. DR1).

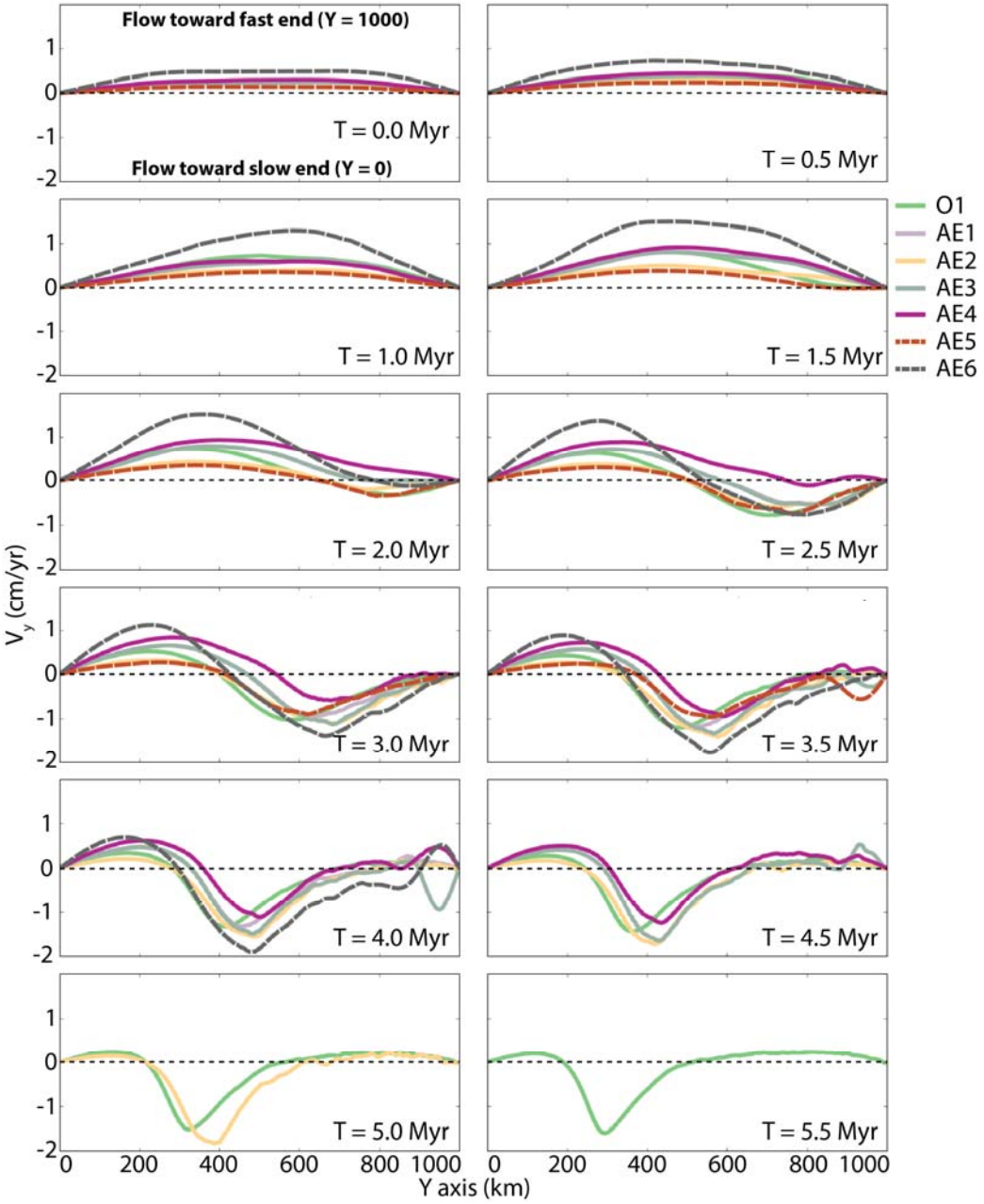

Figure DR4. Sensitivity analyses testing the role of resolution, boundary conditions, and partial melt. The profiles show the velocity component parallel to the rift-axis at the LAB (similar to Figure 4C) of additional experiments run to explore the robustness of experiment setup (see Supplemental Methods for details of each experiment). The additional experiments are all able to reproduce the results from the main text. All models show a similar pattern of initial flow away from the Euler pole, followed by a switch in direction when the asthenosphere approaches its peak height near y = 1000 km. This implies that the large scale mantle dynamics within the models are not dependent on resolution, the boundary conditions, or melt processes. Experiments AE5 (imposed velocities halved) and AE6 (imposed velocities doubled) in particular reinforce the conclusion from the main body of the text. The pattern of initial flow towards the fast end of the model is driven by tectonics (Van Wijk et. al., 2005; Koopmann et. al., 2014): AE5 shows reduced velocities; AE6 shows increased velocities. However, once the asthenosphere has reached its peak, the return flow velocity of

both AE5 and AE6 are relatively consistent with all other experiments, since it is driven by the difference in gravitational potential energy along the rift axis. The larger return flow for AE6 compared to AE5 can be attributed to thermal effects, where the faster rifting leads to weaker asthenospheric material, and hence easier flow, and vice versa. Note that AE5 and AE6 have had their times scaled to match the amount of kinematic extension in each panel.

Figure DR5. Consequences of mapping a spherical velocity field onto a Cartesian domain. **A,** Map view of the model domain at t = 0 Myr, (**A1**), and after 5 Myr of extension (**A2**), The north-south walls are stretched from 1000 to 1006.3 km. **B,** The blue mesh shows the model domain projected in Cartesian (as Underworld models it), and the spherical equivalent (as would be on Earth) shown in a stereographic projection. The red point shows the location of the Euler pole. Black arrows representing the velocity boundary conditions are only shown for the right wall. Notably, in both cases, the applied velocity boundary conditions are parallel to the small circles, as rotation around an Euler pole enforces. The mesh distortion near the Euler pole is evident in the stereographic projection, hence its exclusion from analysis. The Y axis has been adjusted so the Euler pole is at y = 0 km for this figure.

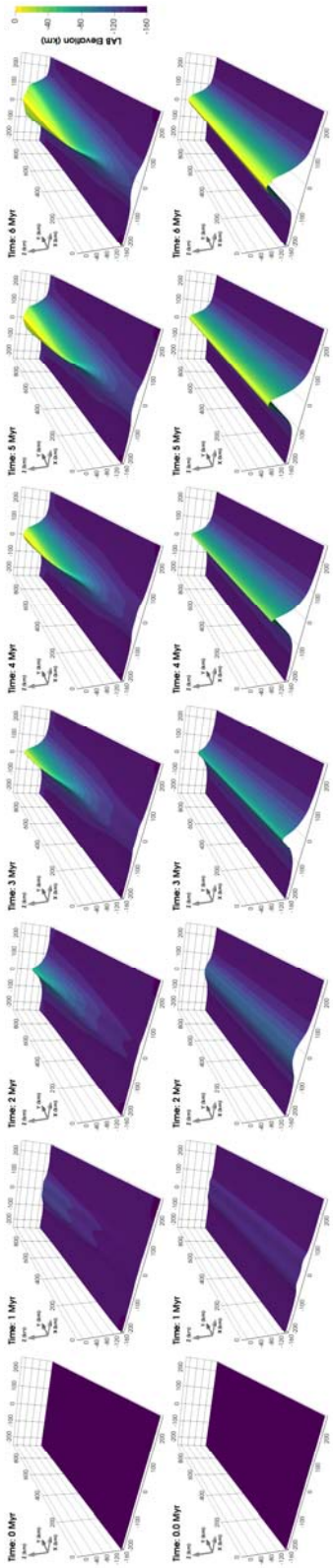

Figure DR6. 3D view through time of the elevation of the lithosphere-asthenosphere boundary (LAB) in the rotational experiment (top) and orthogonal experiment (bottom).

Table DR1

Parameter	**Upper Crust**	**Lower Crust**	**Mantle**
Reference density, ρ_r(kg m^{-3}) at 293.15 K	2800	2900	3300
Thermal expansivity, α (K^{-1})	3e-5	3e-5	3e-5
Heat capacity, C_p(J K^{-1} kg^{-1})	1000	1000	1000
Thermal diffusivity, α(m^2 s^{-1})	1e-6	1e-6	1e-6
Latent heat of fusion, L_f(kJ kg^{-1})	300	300	300
Radiogenic heat production, A (W m^{-3})	1.2e-6	0.6e-6	0.02e-6
Melt density change fraction, $M_{\Delta\rho_r}$	0.13	0.13	0.13
Liquidus term 1, t_1 (K)	1493	1493	2013
Liquidus term 2, t_2 (K Pa^{-1})	-1.2e-7	-1.2e-7	6.15e-8
Liquidus term 3, t_3 (K Pa^{-2})	1.6e-16	1.6e-16	3.12e-18
Solidus term 1, t_1 (K)	993	993	1393.661
Solidus term 2, t_2 (K Pa^{-1})	-1.2e-7	-1.2e-7	1.32899e-7
Solidus term 3, t_3 (K Pa^{-2})	1.2e-16	1.2e-16	-5.104e-18
Friction coefficient	0.577	0.577	0.577
Softened friction coefficient	0.1154	0.1154	0.1154
Cohesion, C (MPa)	10	20	10
Softened cohesion, C (MPa)	2	4	2
Pre-exponential factor, A (MPa^{-n} s^{-1})	6.60693e-8	10e-2	1600
Stress exponent, n	3.1	3.2	3.5
Activation energy, E (kJ mol^{-1})	135	244	520
Activation volume, V (m^3 mol^{-1})	0	0	23e-6
Water fugacity	0	0	1000
Water fugacity exponent	0	0	1.2
Melt viscous softening factor	1e-3	1e-3	1e-1
Melt fraction range for viscous softening	0.2 - 0.3	0.2 - 0.3	0 - 0.02

Code and Experiment Inputs

Numerical code used

The version of *Underworld* used can be found at:

https://github.com/OlympusMonds/EarthByte_Underworld

This version of *Underworld* is a fork of *Underworld 1.8*, with some extras plugins to work more smoothly with the *Lithospheric Modelling Recipe*.

We recommend new users of *Underworld* should use *Underworld 2.0*, found here:
https://github.com/underworldcode/underworld2

Experiment Inputs

The experiments were designed based off the *Lithospheric Modelling Recipe* (the *LMR*), which is a set of pre-defined *Underworld* input files and a script framework to help run them. The *LMR* can be found here:
https://github.com/OlympusMonds/lithospheric_modelling_recipe

The input files used in this experiment can be found here:
https://github.com/OlympusMonds/lmondy-et-al-3D-Rifting-Experiments

References

Crameri, F., Schmeling, H., Golabek, G., Duretz, T., Orendt, R., Buiter, S., May, D., Kaus, B., Gerya, T., and Tackley, P., 2012, A comparison of numerical surface topography calculations in geodynamic modelling: an evaluation of the 'sticky air' method: Geophysical Journal International, v. 189, no. 1, p. 38-54.

Demouchy, S., Tommasi, A., Ballaran, T. B., and Cordier, P., 2013, Low strength of Earth's uppermost mantle inferred from tri-axial deformation experiments on dry olivine crystals: Physics of the Earth and Planetary Interiors, v. 220, p. 37-49.

Dziewonski, A., Chou, T. A., and Woodhouse, J., 1981, Determination of earthquake source parameters from waveform data for studies of global and regional seismicity: Journal of Geophysical Research: Solid Earth, v. 86, no. B4, p. 2825-2852.

Ekström, G., Nettles, M., and Dziewoński, A., 2012, The global CMT project 2004–2010: Centroid-moment tensors for 13,017 earthquakes: Physics of the Earth and Planetary Interiors, v. 200, p. 1-9.

Ellis, S. M., Little, T. A., Wallace, L. M., Hacker, B. R., and Buiter, S. J. H., 2011, Feedback between rifting and diapirism can exhume ultrahigh-pressure rocks: Earth and Planetary Science Letters, v. 311, no. 3-4, p. 427-438.

Floyd, J. S., Tolstoy, M., Mutter, J. C., and Scholz, C. H., 2002, Seismotectonics of mid-ocean ridge propagation in Hess Deep: Science, v. 298, no. 5599, p. 1765-1768.

Hasterok, D., and Chapman, D., 2011, Heat production and geotherms for the continental lithosphere: Earth and Planetary Science Letters, v. 307, no. 1, p. 59-70.

Hirth, G., and Kohlstedt, D., 2003, Rheology of the upper mantle and the mantle wedge: A view from the experimentalists: Inside the subduction Factory, p. 83-105.

Koopmann, H., Brune, S., Franke, D., and Breuer, S., 2014, Linking rift propagation barriers to excess magmatism at volcanic rifted margins: Geology, v. 42, no. 12, p. 1071-1074.

McKenzie, D., and Bickle, M., 1988, The volume and composition of melt generated by extension of the lithosphere: Journal of petrology, v. 29, no. 3, p. 625-679.

Paterson, M., and Luan, F., 1990, Quartzite rheology under geological conditions: Geological Society, London, Special Publications, v. 54, no. 1, p. 299-307.

Rey, P., and Müller, R., 2010, Fragmentation of active continental plate margins owing to the buoyancy of the mantle wedge: Nature Geoscience, v. 3, no. 4, p. 257-261.

Van Wijk, J. W., and Blackman, D. K., 2005, Dynamics of continental rift propagation: the end-member modes: Earth and Planetary Science Letters, v. 229, no. 3-4, p. 247-258.

Wang, Y., Zhang, J., Jin, Z., and Green, H., 2012, Mafic granulite rheology: Implications for a weak continental lower crust: Earth and Planetary Science Letters, v. 353, p. 99-107.

Watremez, L., Burov, E., d'Acremont, E., Leroy, S., Huet, B., Pourhiet, L., and Bellahsen, N., 2013, Buoyancy and localizing properties of continental mantle lithosphere: Insights from thermomechanical models of the eastern Gulf of Aden: Geochemistry, Geophysics, Geosystems, v. 14, no. 8, p. 2800-2817.

Zhong, S., and Watts, A., 2013, Lithospheric deformation induced by loading of the Hawaiian Islands and its implications for mantle rheology: Journal of Geophysical Research: Solid Earth, v. 118, no. 11, p. 6025-6048.